

Searching for the mHz variability in the TESS observations of nova-like cataclysmic variables

A. Dobrotka¹, J. Magdolen¹, and D. Janíková¹

Advanced Technologies Research Institute, Faculty of Materials Science and Technology in Trnava, Slovak University of Technology in Bratislava, Bottova 25, 917 24 Trnava, Slovakia

Received / Accepted

ABSTRACT

Aims. We investigated fast optical variability of selected nova-like cataclysmic variables observed by TESS satellite. We searched for break frequencies (f_b) in the corresponding power density spectra (PDS). The goal is to study whether these systems in almost permanent high optical state exhibit preferred f_b around 1 mHz.

Methods. We selected non-interrupted light curve portions with duration of 5 and 10 days. We divided these portions into ten equally long light curve subsamples and calculated mean PDS. We searched for f_b in frequency interval from $\log(f/\text{Hz}) = -3.5$ to -2.4 . We defined as positive detection when the f_b was present in at least 50% of the light curve portions with a predefined minimum number of detections.

Results. We measured f_b in 15 nova-like systems and confirmed that the value of this frequency is clustered around 1 mHz with a maximum of the distribution between $\log(f/\text{Hz}) = -2.95$ and -2.84 . The confidence that this maximum is not a random feature of a uniform distribution is at least 96%. This is considerably improved since previous value of 69%. We discuss the origin of these f_b in the context of sandwich model where central hot X-ray corona surrounds central optically thick disc. This scenario could be supported by correlation between white dwarf mass and f_b ; the larger the mass, the lower the frequency. We see such tendency in the measured data, however the data are too scattered and based on low number of measurements. Finally, it appears that systems with detected f_b have lower inclination than 60–75°. In higher inclination binaries the central disc is not seen and the PDS is dominated by red noise. This also supports the inner disc regions as source of the observed f_b .

Key words. accretion, accretion discs - stars: novae, cataclysmic variables - stars: white dwarfs

1. Introduction

Cataclysmic variables (CVs) are interacting binaries powered by an accretion process. The mass is transferred from a main sequence companion star via Roche lobe overflow, and in the absence of a strong magnetic field, an accretion disc forms (see e.g. Warner 1995 for a review). In any case, the matter flows towards the central white dwarf (WD).

In CVs we distinguish between high and low optical brightness states based on the mass accretion rate \dot{m}_{acc} through the disc. The physical conditions in these states are defined by hydrogen ionisation, and the alternation between these two states observed mainly in dwarf novae is generated by viscous-thermal instability (Osaki 1974; Hōshi 1979; Meyer & Meyer-Hofmeister 1981). In the low state the disc is cold, the hydrogen is recombined and \dot{m}_{acc} is low. During the high state, the hydrogen is ionised in the hot disc and is brighter in the optical due to the larger \dot{m}_{acc} compared to the low state. The accretion disc is fully developed (almost) up to the WD in the high state, while it is truncated in the low state. This truncation explains delays between optical, UV radiation and X-rays (see e.g. Schreiber et al. 2003).

CVs with mass transfer from the secondary high enough, spend most of their lifetime in a high state. This is due to \dot{m}_{acc} being above a critical value, and the viscous-thermal instability does not appear. This larger matter flow

through the disc ensures an almost permanently hot disc with ionised hydrogen and dwarf nova outbursts suppression. Such CVs systems are called nova-likes. Fluctuations in mass transfer from the secondary, probably due to star spots, occasionally appear, and the nova-like system falls to a low state for a relatively short time (Honeycutt & Kafka 2004). Such behaviour is described as antidwarf novae and is typical for VY Scl nova-like systems.

Typical manifestation of the underlying accretion process is fast stochastic variability called flickering. This variability exhibits variety of observational features with the most important being: (1) linear correlation between variability amplitude and log-normally distributed flux (so called rms-flux relation) (see Scaringi et al. 2012b; Van de Sande et al. 2015), (2) power density spectra (PDS) with the shape of a red noise or band limited noise with characteristic frequencies in the form of a break or Lorentzian (Scaringi et al. 2012a; Dobrotka et al. 2016) and (3) time lags, in which the flares reach their maxima slightly earlier in the blue than in the red (Scaringi et al. 2013; Bruch 2015).

The characteristic frequencies in the PDSs bring information about time scales of physical processes generating the variability. Some systems show a single break frequency f_b in the PDS like UU Aqr (Baptista & Bortoletto 2008) or KR Aur (Kato et al. 2002). Usually, these detections are made using ground observations. For de-

tection of multicomponent PDS a long and uninterrupted light curve is needed. This is the case of *Kepler* spacecraft, which allowed to detect various components in MV Lyr (Scaringi et al. 2012a), V1504 Cyg (Dobrotka & Ness 2015) and V344 Lyr (Dobrotka et al. 2016). X-ray observations yielded also detections of single or multicomponent PDSs. Examples of single-component PDSs are VW Hyi, WW Cet, T Leo (Balman & Revnivtsev 2012), while SS Cyg (Balman & Revnivtsev 2012), RU Peg (Dobrotka et al. 2014) or MV Lyr (Dobrotka et al. 2017) exhibit more complex PDS morphology.

Dobrotka et al. (2020) summarized various detections of characteristic frequencies of flickering in the PDSs of CVs. The study implies that two characteristic frequencies can exist in the low state. The same is seen in the high state, but together with an additional third most prominent component at $\log(f/\text{Hz}) \simeq -3$. However, the study summarized only 12 detections, and the corresponding frequency distribution can be easily explained by the random appearance of a uniform distribution. More detections are needed to construct a significant histogram.

Dobrotka et al. (2021) found another system exhibiting the $\log(f/\text{Hz}) \simeq -3$ signal as a clear f_b in *Kepler* data. However, the system is an intermediate polar (IP) V4743 Sgr with a magnetic WD. Such magnetic CVs have truncated discs which makes them different from non-magnetic nova-like CVs. f_b with values close to or higher than $\log(f/\text{Hz}) \simeq -3$ were detected in other IPs (Revnivtsev et al. 2010; Semena et al. 2014). The detected f_b are very close to WD spin values. If the inner truncated disc edge is co-rotating with the central WD, this explains the similarity of the break and spin frequency. Therefore, such f_b at $\log(f/\text{Hz}) \simeq -3$ is non-associated to the flickering activity in CVs. However, V4743 Sgr is rather special IP. It is a nova remnant where the mass transfer rate is quite high, and the inner disc edge should be pushed much closer to the WD, and further away from the co-rotating radius. Therefore, the detected f_b can still be associated to the flickering activity, even if its value is close to the WD spin.

In order to test the hypothesis about preferred characteristic frequencies in CVs in high and low state, new PDSs studies are needed. The probability that the characteristic frequency $\log(f/\text{Hz}) \simeq -3$ is preferred is only 69% so far (Dobrotka et al. 2021). With a questionable magnetic V4743 Sgr the probability rises to 91%.

Scaringi (2014) interpreted the main feature at $\log(f/\text{Hz}) \simeq -3$ detected in optical *Kepler* data of MV Lyr as being due to a hot, geometrically thick disc (hot X-ray corona) surrounding a cool, geometrically thin disc (the so called sandwich model). Such corona consists of evaporated gas from the underlying geometrically thin disc (Meyer & Meyer-Hofmeister 1994). It radiates in X-rays, and these X-rays are reprocessed into optical by the geometrically thin disc. The physical origin of the variability is explained by propagating mass accretion fluctuations (Lyubarskii 1997; Kotov et al. 2001; Arévalo & Uttley 2006) in the corona.

However, the ratio of X-ray to optical luminosity is on the order of 0.1 (see e.g. Dobrotka et al. 2020), which is too low to explain the observed optical and UV variability with a reprocessing scenario. Dobrotka et al. (2019) studied the shot profile of the flickering in the *Kepler* data of MV Lyr. The authors found two components with different amplitudes in the averaged shot profile. Both having char-

acteristic frequencies of $\log(f/\text{Hz}) \simeq -3$. While the component with high amplitude (central spike) is problematic to be generated by the reprocessing, the low amplitude side-lobes match the scenario (Dobrotka et al. 2020). This suggests that the variability is formed in two separate regions: the geometrically thin disc, and the reprocessed X-rays of the geometrically thick corona.

Apparently, the origin of the flickering variability is not yet understood, and further study is needed. Our goal is to increase the number of measured PDS characteristic frequencies. The corresponding distribution of frequency values can have substantial impact on flickering understanding, like it was in the case of orbital period distribution (see Warner 1995 for review). In this paper we searched for f_b in PDSs calculated from TESS data of nova-like CVs.

2. Selected systems and observations

In this paper we present analysis of TESS light curves of all nova-like and old nova systems listed in the Bruch (2022), Bruch (2023a) and Bruch (2023b). The Pre-search Data Conditioning Simple Aperture Photometry (PDCSAP) light curves were downloaded¹ from the Mikulski Archive for Space Telescopes (MAST) with cadence of 120 seconds as with PDCSAP flux long term trends are removed.

3. PDS analysis

We searched for characteristic f_b in PDSs calculated from the selected light curves. Since *Kepler* spacecraft is much superior instrument, the corresponding PDSs showed multicomponent character in several cases (Scaringi et al. 2012a; Dobrotka et al. 2016). The TESS case is considerably worse, and only the dominant f_b can be seen. Moreover, selected nova-like CVs show superhump or orbital periods longer than 0.06 day (Bruch 2022, 2023a,b). This corresponds to frequency of $\log(f/\text{Hz}) = -3.7$ and lower. Such frequency can affect the observed PDS and lead to wrong identification or measurement of f_b . However, we are interested mainly in high frequency component close to $\log(f/\text{Hz}) \simeq -3$. Therefore selecting frequency interval from $\log(f/\text{Hz}) = -3.5$ to higher frequencies resolve the potential superhump or orbital period contamination problem.

3.1. Method

We first selected suitable light curve portions for PDS calculation. To avoid large gaps in the data, we selected only the segments between them. We defined a gap as a duration of 0.2 days or more. This limit was determined empirically, as using this threshold all obviously large gaps were eliminated. Fig. 1 shows two examples of this selection process.

Second step is to select the light curve portions with duration of n_d days. Empirically derived optimal value is 10. However, not all of the examined objects have such uninterrupted 10 days intervals. Therefore, we performed analysis using $n_d = 5$ and 10. We could use the whole light curve portion between the gaps, but we prefer to have all

¹ Using Python Lightkurve library; <https://docs.lightkurve.org>.

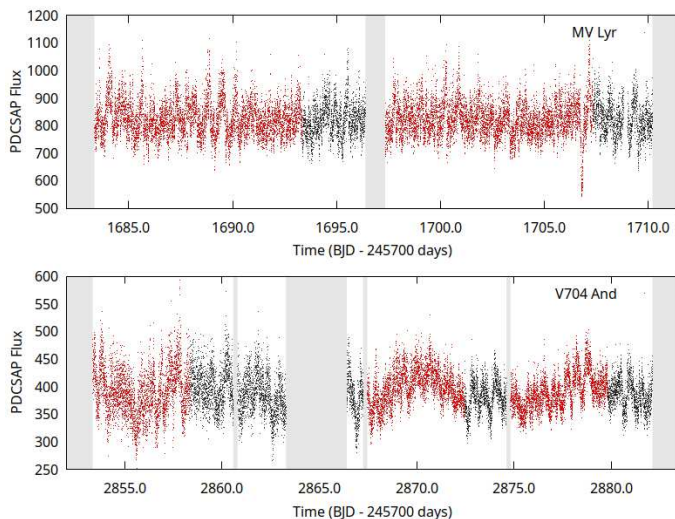


Fig. 1. Examples of light curves (black points) with gaps (gray shaded areas) and selected portions (red points) with duration of 10 (upper panel) and 5 (lower panel) days for PDS analysis.

PDSs equivalent with the same frequency resolution and PDS point step.

To estimate the PDS we divided each light curve portion into n_{subs} subsamples. For each subsample, we calculated a periodogram using the Lomb-Scargle algorithm² (Scargle 1982). All periodograms (power³ p as a function of frequency f) were subsequently transformed into log-log space. Averaging of $\log(p)$ instead of p is recommended by Papadakis & Lawrence (1993). The whole $\log(f)$ interval of the PDS we re-binned with a constant frequency step of 0.1 dex. Finally, all $\log(p)$ points within each frequency bin were averaged. We defined an additional condition for averaging; the number of averaged periodogram points per bin must be larger than some pre-selected value defined as $n_{\text{min}} \times n_{\text{subs}}$ (n_{min} points from each of n_{subs} periodograms). If the condition is not valid, the bin should be broadened until the condition is fulfilled. This allows us to get enough points for mean value with standard error of the mean calculation.

The PDS frequency resolution and the lowest PDS frequency (before re-binning) are proportional to the duration of the light curve subsamples. Therefore, an empirical compromise between noise and resolution must be found. As n_{subs} and $n_{\text{min}} \times n_{\text{subs}}$ values we chose 10 and 3×10 , respectively. The high-frequency end of the periodogram is set by the Nyquist frequency.

We fitted the resulting PDSs with a broken power law model using the `GNUPLOT`⁴ software. The selected frequency range was from $\log(f/\text{Hz}) = -3.5$ to -2.4 .

3.2. Selection of positive detections

First step is to identify systems with PDS contaminated by other signals not associated to flickering. Superhumps and

orbital periods are no longer a complication, as described above. However, IPs like AO Psc and IGR J08390-4833 have spin frequencies of $\log(f/\text{Hz}) = -2.91$ (van der Woerd et al. 1984) and -3.16 (Sazonov et al. 2008), respectively. This clearly affects the studied PDSs (left panel in Fig. 2). These systems we excluded from the analysis.

Second step is to select objects with positive f_b detections. Systems, where the PDS is dominated by white (second panel of Fig. 2) or red noise (third panel of Fig. 2) did not yield any detection. More problematic are the cases, where random features or noise in the PDS can mimic the searched f_b . For this reason we selected only those PDSs, where f_b is persistent and stable. This means, that it must be detected various times and with similar values. For this selection process we relied on well studied MV Lyr (Scaringi et al. 2012a). The detection of f_b close to $\log(f/\text{Hz}) = -3$ is unambiguous thanks to the *Kepler* observations. After inspecting individual PDSs from the TESS light curves, we selected only those light curve subsamples where the detected f_b has an error of 0.10 or less⁵. Larger errors occurred in cases of clearly scattered and noisy PDSs (right panel in Fig. 2) or where the break was not obvious, making the broken power law shape is untrustworthy. Moreover, if the PDSs did not show the broken power law shape at all, the fit did not converge to such a shape, and the f_b reached the end with absurd errors. This selection process yield 19 detections of f_b out of 27 light curve subsamples with $n_d = 5$, and 10 detections out of 13 light curve subsamples with $n_d = 10$. Therefore, the fraction of positive detections n_p is 70% and 77% for $n_d = 5$ and $n_d = 10$, respectively. Apparently, the persistent f_b in MV Lyr is not detected in all light curve subsamples probably due to limited capabilities of TESS yielding more scattered PDSs compared to the *Kepler* results. Therefore, as positive detections in all other systems we choose cases where n_p parameter was at least 50%. However, if the total number of light curve subsamples is only two, the detection of a single f_b is not sufficient. Therefore, we considered a detection to be positive if at least two f_b were detected. More strict condition will be applied later.

3.3. Results

Fig. 3 shows selected examples of PDSs with fits for objects where we found positive detections. Fig. 5 shows measured f_b with errors for all positive detections. Both n_d of 5 and 10 are shown. As previously mentioned, the $n_d = 5$ case is more scattered than $n_d = 10$. Therefore, we rely on $n_d = 10$ if possible. Only TT Ari and V704 And does not have uninterrupted light curve portions long enough and only $n_d = 5$ cases are shown. To judge whether the scatter of measurements is acceptable or not, we again used the well studied MV Lyr as a benchmark. The $n_d = 10$ measurements scatter between values $\log(f/\text{Hz}) = -2.79$ and -3.09 . All points are randomly redistributed around the value of $\log(f/\text{Hz}) = -2.9$, and only the last point (measurement 10) is slightly deviated toward higher frequencies. We investigated the long term AAVSO light curve and concluded that

² We used python's package `Astropy` (Astropy Collaboration et al. 2013, 2018, 2022).

³ We use power normalized by the total variance according to Horne & Baliunas (1986). Since the normalization does not affect the shape of the PDS, this has no importance in our case.

⁴ <http://www.gnuplot.info/>

⁵ Since this error limit is more or less approximate and empirically estimated, we took all values rounded to 0.10, therefore up to 0.10499... This allowed us to get five additional measurements. This was useful mainly in AH Men case where it helped to fulfill the $n_p = 50\%$ condition.

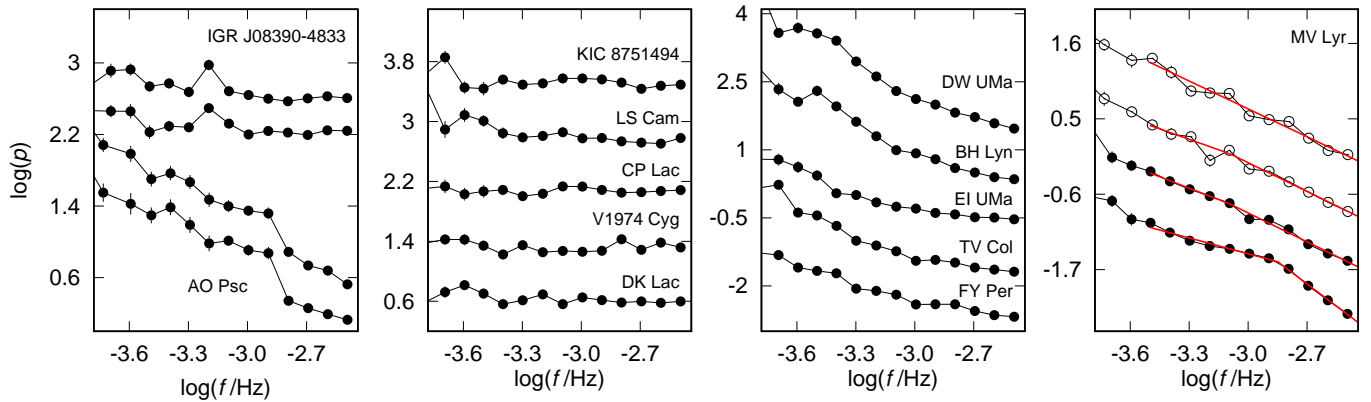


Fig. 2. Examples of PDSs. Black points represent PDSs with $n_d = 10$ and black circles are for $n_d = 5$. First (left) panel - IPs with strong spin frequency affecting the PDS. Second panel - example of PDSs dominated by white noise. Third panel - example of PDSs dominated by red noise. Fourth (right) panel - Examples of PDSs of MV Lyr with broken power law fits. The upper PDS shows case where the fitting process did not converge to the broken power law shape. There is no f_b but a straight line instead. The middle two cases represent possible positive detection but with f_b error larger than 0.10. Apparently, the f_b is not clear even if the fit converged. The lower case is an example of a positive detection with a small enough error of the f_b due to clear broken power law shape of the PDS. Individual PDSs are offset vertically for better visualisation.

this measurement was made during a transition from a high to a low state (Fig. 4). Dobrotka et al. (2020) showed that the f_b increases during such transition, therefore the deviation toward higher frequencies is natural. Since we need stationary data, we excluded this measurement from our analysis. The last but one observation is not made during the "standard" high state before day MJD = 2400, but apparently it occurred during a stable plateau. The brightness differs from that of all other observations, but since it is stabilised, the disc probably has all the physical characteristics of the "standard" high state. Finally, the measured f_b shows no suspicious deviation. All other TESS observations were taken during the "standard" high state. Therefore, as measurement scatter we take the frequency interval from $\log(f/\text{Hz}) = -2.85$ to -3.09 (gray shaded area). Based on more precise measurements using the superior space-craft *Kepler* this scatter is natural and represents the well known f_b at approximately $\log(f/\text{Hz}) = -3$ (f_2 in Fig. 1 from Dobrotka et al. 2020).

Let's see the Fig. 5. As a priority we take and describe the $n_d = 10$ case. This is not possible only for TT Ari and V704 And where we rely on $n_d = 5$ data. All measurements lie within the gray shaded area except AH Men and already discussed MV Lyr. AH Men falls very well to the scatter interval too except one single point (11th measurement). The AAVSO light curve is not covered enough to judge whether the system experienced similar brightness transition like MV Lyr. Anyhow, all other measurements are robust, therefore we excluded the deviated point from all subsequent analysis and discussions. All measured and selected f_b values displayed in Fig. 5 are summarised in Tables A.1 and A.2.

To test the hypothesis from Dobrotka et al. (2020) regarding the prevalence of f_b at approximately $\log(f_b/\text{Hz}) = -3$, we calculated a histogram representing the statistical distribution of measured f_b values from $\log(f_b/\text{Hz}) = -3.4$ to -2.5 ⁶. For this purpose we used weighted averages of measured f_b values using $n_d = 10$ preferentially. This averages

⁶ Since the fit is performed on interval from $\log(f_b/\text{Hz}) = -3.5$ to -2.4 , the break frequency cannot fall to the boundaries.

Table 1. Weighted averages of measured f_b for individual systems used for calculation of histograms in Fig. 6.

object	$\log(f_b/\text{Hz})$	n_d	n_m	n_p (%)
AH Men	-2.813 ± 0.017	10	12	52
BB Dor	-3.145 ± 0.008	10	28	97
KQ Mon	-3.159 ± 0.049	10	2	100
KR Aur	-2.778 ± 0.018	10	6	100
MV Lyr	-2.937 ± 0.012	10	10	77
QU Car	-3.321 ± 0.027	10	2	50
TT Ari	-3.105 ± 0.009	5	11	100
V504 Cen	-2.860 ± 0.046	10	2	100
V592 Cas	-2.853 ± 0.020	10	3	100
	-2.881 ± 0.009	5	14	100
V704 And	-2.939 ± 0.026	5	4	80
V751 Cyg	-2.982 ± 0.023	10	2	100
	-2.989 ± 0.017	5	7	70
V795 Her	-2.923 ± 0.041	10	2	100
	-2.913 ± 0.021	5	5	83
V1193 Ori	-2.849 ± 0.019	10	3	75
	-2.852 ± 0.013	5	5	63
HS 0506+7725	-2.866 ± 0.012	10	7	58
TIC 92167387	-3.008 ± 0.061	10	2	100

Notes. See text for details about the use of n_d and n_m for selection.

are summarised in Table 1. The corresponding histograms with 8 bins⁷ are depicted in upper panels of Fig. 6.

First we show all systems from Fig. 5 (upper left panel). This case is based on systems with minimal number of selected f_b measurements equal to two. Such number is too low to judge whether the f_b is stable or not. Larger criterion would be better to increase the confidence of the histogram. However, the larger this criterion, the lower the number of systems in the histogram. This is at the expense of the histogram resolution. Nevertheless, we show also such more conservative case with minimal number of f_b measure-

⁷ Comparable to Fig. 11 in Dobrotka et al. (2020).

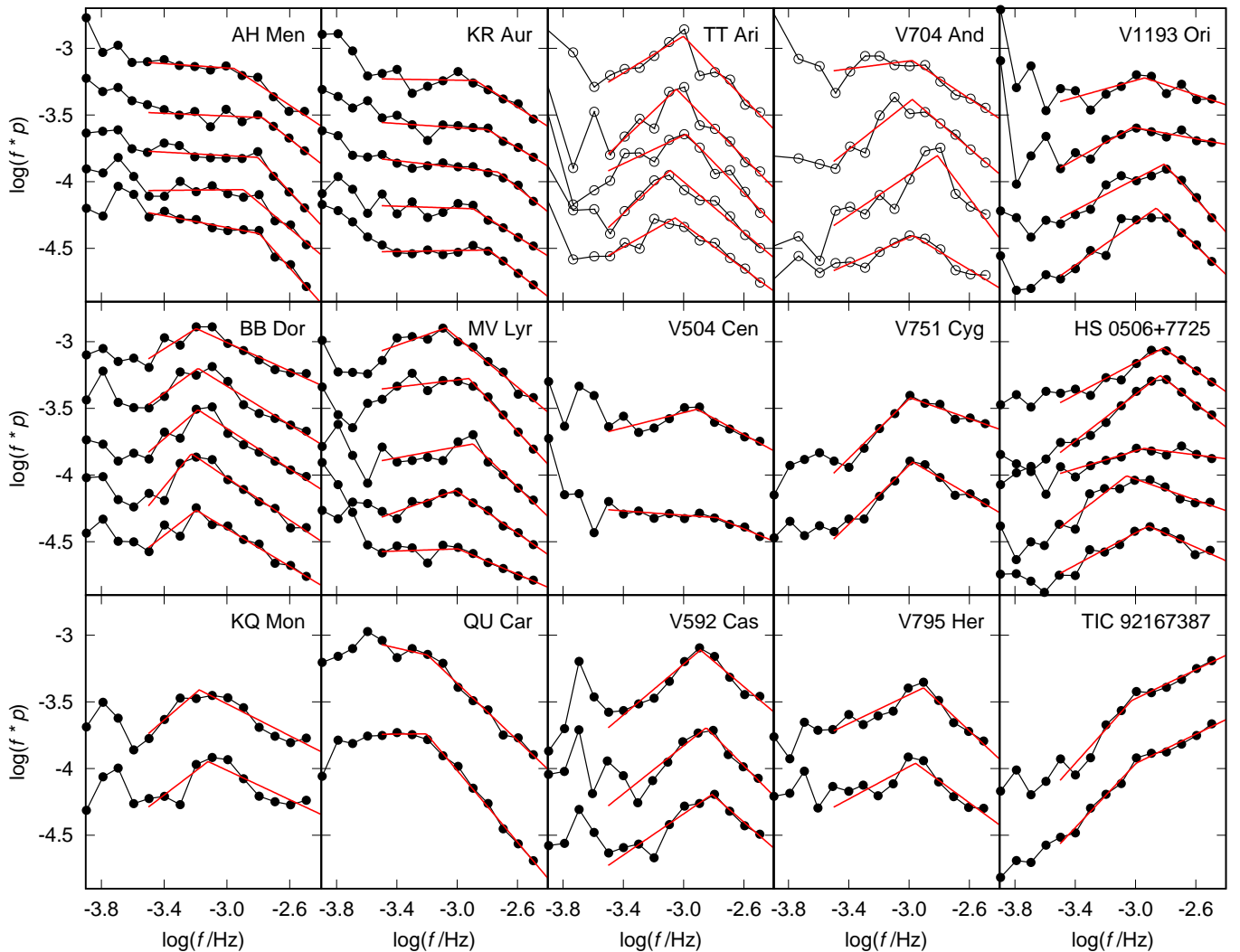


Fig. 3. Examples of PDSs for individual systems with broken power law fits (red lines). Black points represent PDSs with $n_d = 10$ and black circles are for $n_d = 5$. Individual PDSs are offset vertically for better visualisation.

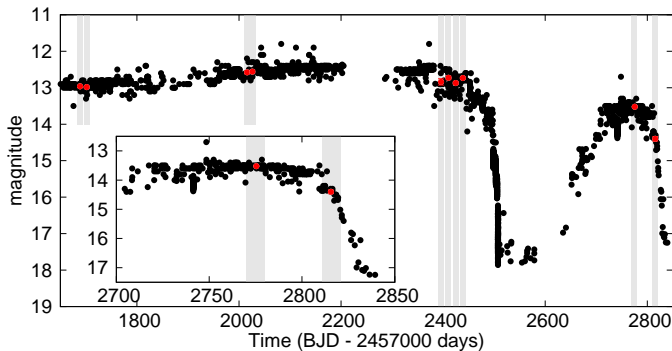


Fig. 4. AAVSO light curve of MV Lyr with marked observation intervals of TESS by gray shaded areas. The inset panel shows a detail of the two most recent TESS observations falling before and at the beginning of the decline from the high optical state. Red points are mean brightness of the AAVSO data during the TESS observations.

ments equal to five. Focusing primary on the $n_d = 10$ condition this excludes KQ Mon, QU Car, TT Ari, V504 Cen, V592 Cas, V704 And, V751 Cyg, V795 Her, V1193 Ori and TIC 92167387. If $n_d = 10$ case did not satisfy the condition

of minimal detections of five, we used $n_d = 5$ case instead. This brings back TT Ari, V592 Cas, V751 Cyg, V795 Her and V1193 Ori. The corresponding histogram is in the upper right panel of Fig. 6.

4. Discussion

We investigated the optical flickering of CVs in high optical state. For this purpose we selected nova-like systems observed by TESS satellite. We searched for break frequency f_b in corresponding PDSs. The goal was to increase the low number (just five) of detections in Dobrotka et al. (2020). We found 13 new (15 in total) systems with positive detections of f_b . Histograms in Fig. 6 depict the resulting statistics.

4.1. PDS break frequency

Dobrotka et al. (2020) formulated a hypothesis that CVs in high state have a preferable f_b close to $\log(f/\text{Hz}) = -3$. The Fig. 6 supports this possibility. Apparently, the measurements cluster and culminate close to $\log(f/\text{Hz}) = -3$. The upper panels show the detections from this work, while the lower panels depict the statistics after including additional

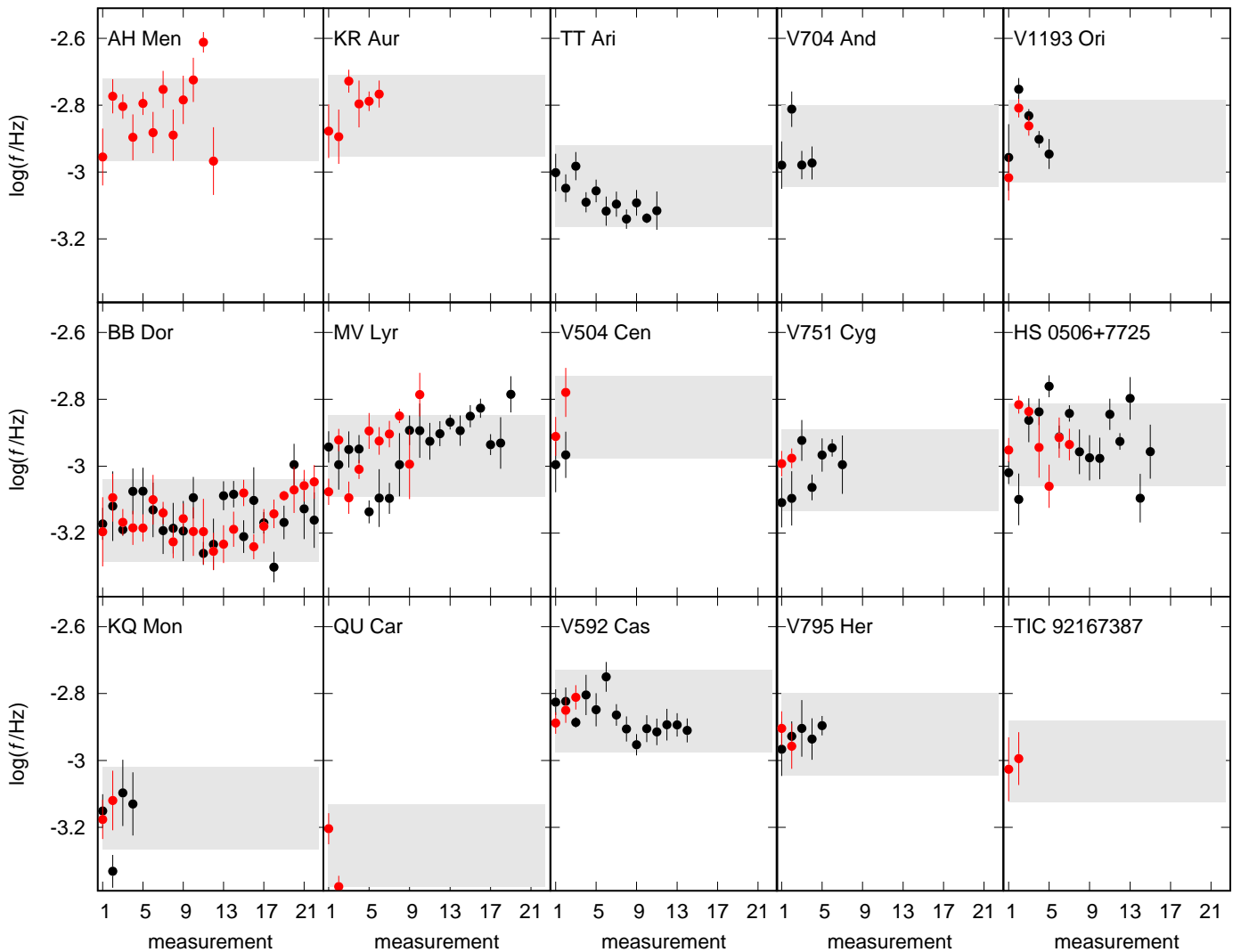


Fig. 5. Measurements of f_b where conditions for positive detection were satisfied (see text for details). Red and black points represent the $n_d = 10$ and 5 case, respectively. Grey shaded area is the natural scatter based on MV Lyr case. BB Dor case is not fully displayed for clarity, but the hidden measurements have the same scatter as shown (compared to gray shaded area).

MV Lyr⁸, KR Aur, V1504 Cyg, V344 Lyr and V4743 Sgr values from Table 2 of Dobrotka et al. (2020). UU Aqr is not added because it is out of studied frequency range from $\log(f/\text{Hz}) = -3.4$ to -2.5 .

The only problematic is V4743 Sgr, identified as an intermediate polar with magnetic WD (Ness et al. 2003; Kang et al. 2006). Such magnetic CVs have truncated discs with the inner disc edge responsible for observed f_b very close to the $\log(f/\text{Hz}) \simeq -3$ or higher (Revnivtsev et al. 2010; Semena et al. 2014). Usually, these f_b are close to the spin frequency of the WD. This is also the case of V4743 Sgr (Dobrotka et al. 2021). This means that the measured f_b can be of different origin than the studied flickering in non-magnetic CVs like in this work. However, all IPs have disc in the low state (Hameury & Lasota 2017), while Dobrotka et al. (2021) suggests that the disc in V4743 Sgr is in a high state making this IP different from "standard" IPs. It is a post-nova. Therefore, it is possible that the measured f_b has different origin than in "standard"

IPs, and it represents the studied flickering. But since this is only a possibility, we mark it as a red line in Fig. 6.

The histogram in Fig. 6 is divided into 8 equally spaced bins with slightly narrower frequency extension than used in Dobrotka et al. (2020). This different spacing with slightly better resolution (0.113 vs. 0.144) allows to better identify the f_b , which is between $\log(f/\text{Hz}) = -2.95$ and -2.84 . Question is whether the observed dominant bin in the histogram represents a preferred or most frequent value, or it is just a random feature of a uniform distribution. Dobrotka et al. (2021) simulated such a histogram with a uniform distribution and concluded that 31% of simulations yield at least one bin with an equal or larger height than the dominant bin in their Fig. 11. This means that the statement that the dominant bin represents a preferred frequency has a confidence of only 69%. Adding the V4743 Sgr case this confidence increases to 91%.

With the new histogram in Fig. 6, we see that the V4743 Sgr case do not fall into the dominant bin, and therefore does not increase the estimated confidence. We performed the same simulations as Dobrotka et al. (2021), and after one million repetitions, we got confidences of 99 and

⁸ For MV Lyr we added only values of $\log(f/\text{Hz}) = -3.3$ and -2.5 , because f_b close to $\log(f/\text{Hz}) = -3$ was used from this work.

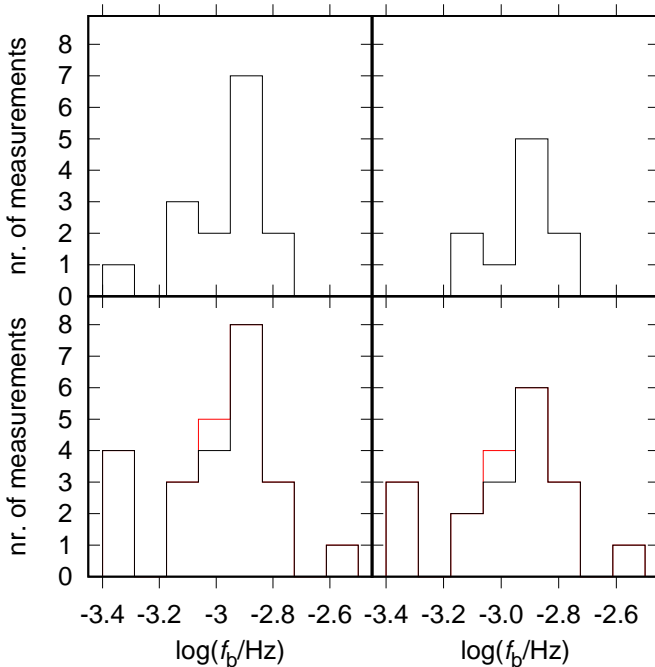


Fig. 6. Histograms of weighted means (number of measurements) of f_b of individual systems. Left panels - systems with minimal number of selected f_b equal to two (AH Men, BB Dor, KQ Mon, KR Aur, MV Lyr, QU Car, TT Ari, V504 Cen, V592 Cas, V704 And, V751 Cyg, V795 Her, V1193 Ori, HS 0506+7725, TIC 92167387). Right panels - systems with minimal number of selected f_b equal to five (AH Men, BB Dor, KR Aur, MV Lyr, TT Ari, V592 Cas, V751 Cyg, V795 Her, V1193 Ori, HS 0506+7725). Upper panels - measurements from this paper. Lower panels - same as upper panels but with added measurements from other works. Red line represents the uncertain V4743 Sgr case.

96% using only TESS detections from this work for a minimal number of two and five f_b measurements (upper panels of Fig. 6), respectively. Adding all other measurements except V4743 Sgr (lower panels of Fig. 6) yield confidences of 96 and 85%. Finally, adding also the questionable post-nova yields values of 95 and 81%.

Apparently, the worst case is 81%, but excluding the uncertain V4743 Sgr it is 85%. Therefore, we got a significant increase in confidence compared to the original 69%, but still not enough for a definite conclusion, unless we want to rely on the less conservative case with a minimal number of f_b measurements of two. Nevertheless, we must be cautious in adding measurements from different instruments. If TESS is able to detect only the dominant f_b in MV Lyr, and *Kepler* is able to see fainter PDS structures, we may discuss the dominant value close to $\log(f/\text{Hz}) = -3$, but it may be confusing to judge the statistical significance of the presence of other frequencies detected by *Kepler* only. Therefore, it is best to rely on measurements from this work based on TESS observations only. In such a case, the more conservative approach yield a confidence of 96%. This is already high enough to conclude that nova-like CVs have very probably a preferred f_b between $\log(f/\text{Hz}) = -2.95$ and -2.84. Whether it is really a kind of preferred value or just a maximum in a smooth f_b distribution is not known yet due to the low number of f_b measurements.

4.2. Dependence on physical parameters

The next step is to understand the physical meaning of such a preferred value or distribution maximum. The best way is to search for a correlation of the f_b with basic physical parameters. Comparing f_b values with orbital periods did not yield any correlation. The data show just a scattered cloud of points. This is not surprising because the flickering in CVs and related objects is usually associated with the accretion disc and especially its inner regions (Bruch 1992, 1996; Zamanov & Bruch 1998; Bruch 2000; Baptista & Bortolotto 2004; Scaringi 2014), while the orbital period is more typically associated with the secondary star characteristics (Smith & Dhillon 1998).

The inner disc region potentially connected to the flickering is the inner disc edge. Balman & Revnivtsev (2012) suggests that the f_b represents the Keplerian frequency at this inner disc edge. If true, the f_b should be higher in the high state compared to the low state. However, opposite is observed in the case of nova-like MV Lyr (Dobrotka et al. 2020). Nova-likes in the high state are similar to dwarf novae in outburst where the inner disc is build down to the WD surface or close to it. Once the CV changes states, the disc starts to be truncated and the Keplerian frequency should decrease during the transition. Opposite was observed in the transition of MV Lyr detected by the *Kepler* spacecraft. The dominant f_b at $\log(f/\text{Hz}) = -3$ increased together with another one or two adjacent PDS components. Anyhow, this does not tell us anything about the preference of any f_b value. Even if the f_b is generated by the inner disc edge, the preference would suggest some preferred inner disc radius. It is hard to test such a statement because measurements of the inner disc radii are rare.

An alternative interpretation is the sandwich model with a inner hot corona. Based on the accretion fluctuation propagation model an accretion inhomogeneity forms somewhere in the disc and propagates inwards. Such fluctuation follows the local physical conditions and local viscous time scale. Further away from the center is such fluctuation generated, larger is the corresponding time scale. If the fluctuations are generated in the inner corona, the outer radius of such geometrically thick disc determines the largest time scale of the fluctuations. Therefore, the larger the corona outer radius, the lower the f_b (Fig. 3 in Scaringi 2014). This may explain the increase of f_b during the transition of MV Lyr from high to low state. If \dot{m}_{acc} decreases during such a transition, the energy generation decreases too. Lower energy yields lower matter evaporation and the corona may shrink. As a consequence, this shrinking generates an increase of f_b . Similar reasoning may be applied when considering mass of the central WD m_{WD} . A larger m_{WD} generates a deeper potential well. This results in higher temperatures of the inner disc and the corona can be evaporated to further distances from the center. Such a more radially extended corona should generate a lower f_b .

To test the m_{WD} scenario, we need to collect the masses measurements. In the case of nova-likes this is not easy because the accretion rate is too high to allow detection of a WD even at UV wavelengths. An accretion disc model or a combination of it with a WD model can be used instead. AH Men was studied using IUE spectroscopy (Gänsicke & Koester 1999). Unfortunately, the determined m_{WD} is not unambiguous due to conflicts with distance constraints. The disc modelling yields values of

0.35 and $0.55 M_{\odot}$. We use a mean value of $0.45 \pm 0.10 M_{\odot}$. Godon et al. (2008) studied FUSE spectra of BB Dor and disc modelling derived a m_{WD} of $0.8 M_{\odot}$. KQ Mon m_{WD} was determined by Wolfe et al. (2013) using archival IUE spectra. Its value from disc modelling is estimated to $0.6 M_{\odot}$. KR Aur has several m_{WD} estimates. Shafter (1983) used somewhat controversial method (as stated by the authors) using radial velocities and estimated value of $0.7 M_{\odot}$ using spectra from ground observations. Mizusawa et al. (2010) used IUE spectra and derived slightly lower mass of $0.6 M_{\odot}$ using combination of disc and WD model. These two estimates agree well with another value of $0.59 \pm 0.17 M_{\odot}$ from Ritter & Kolb (2003) catalogue. Most recently, Rodríguez-Gil et al. (2020) used GTC spectra during low state, during which the WD is dominant and well seen. They derived quite a different mass from the previous estimates with a value of $0.94^{+0.15}_{-0.11} M_{\odot}$. For MV Lyr Hoard et al. (2004) derived a mass of $0.73 \pm 0.10 M_{\odot}$ from FUSE spectroscopy using a combined WD + disc model. The system was observed in a low state, therefore the spectrum was dominated by the WD features. m_{WD} of QU Car was determined using combined FUSE, HST and IUE spectra (Linnell et al. 2008). Non-standard accretion disc model yields m_{WD} between 0.6 and $1.2 M_{\odot}$. We use a mean value of $0.9 \pm 0.3 M_{\odot}$. m_{WD} in TT Ari can be estimated as $0.57 M_{\odot}$ using spectra from ground observations and applying disc plus additional black body model (Belyakov et al. 2010). Huber et al. (1998) used photometric and spectroscopic data to study system parameters of V592 Cas. The authors acknowledge that the method they used is criticised by several other authors⁹. Their estimated m_{WD} is $1.4^{+1.0}_{-0.6} M_{\odot}$. We take $1.4 M_{\odot}$ as an upper limit due to Chandrasekhar limit. Finally, WD of V795 Her has a mass of approximately $0.8 M_{\odot}$ by Mizusawa et al. (2010) using IUE spectra and disc + WD atmosphere model. All values are summarised in Table. 2.

Upper panel of Fig. 7 shows the correlation between m_{WD} and f_b of the mentioned systems. The first view is rather uncertain. Ignoring the problematic measurements shown by red color, mainly the V592 Cas case, the situation is clearer. Only the too scattered KR Aur complicates the judgement. Without the highest m_{WD} estimate there is a tendency to see the anticipated correlation. f_b decreases with increasing m_{WD} . The scatter of points is relatively large, but this is natural because determination of m_{WD} is very uncertain and is usually done with large errors. Therefore, we cannot definitely conclude whether the correlation is real or if the redistribution of points is just random. There are three ways of answering whether the correlation is real. We should either refine or revise m_{WD} of KR Aur and QU Car, increase the number of measured f_b for systems with known m_{WD} , or to get f_b measurements for CVs with high m_{WD} (above $1 M_{\odot}$) to populate upper right region of upper panel of Fig. 7.

If f_b is really correlated with m_{WD} , the preferred value between $\log(f/\text{Hz}) = -2.95$ and -2.84 suggests existence of a preferred m_{WD} . Zorotovic et al. (2011) studied the m_{WD} distribution in CVs and their Fig. 7 shows a maximum at $0.8 M_{\odot}$. This can represent the mentioned preferred value, and in such case it would be just a maximum of an otherwise smooth distribution. Best way to check whether the

⁹ It is the same method as used for KR Aur by Shafter (1983) where the authors acknowledge the problematic aspect.

Table 2. Used system parameters.

object	m_{WD} (M_{\odot})	\dot{m}_{acc} (M_{\odot}/yr)	i (deg)
AH Men	$0.35/0.55^a$	$3 \times 10^{-10}^a$	20^a
BB Dor	0.8^b	10^{-9}^b	$<10^b$
KQ Mon	0.6^c	10^{-9}^c	$60 - 75^c$
KR Aur	0.7^d 0.6^e 0.59 ± 0.17^f $0.94^{+0.15}_{-0.11}^g$	$3 \times 10^{-10}^e$	$<40^d$ 41^e 38^f 47^g
MV Lyr	0.73 ± 0.10^h	$3 \times 10^{-9}^i$	12^h
QU Car	$0.6 - 1.2^j$	$10^{-7} - 10^{-6}^j$	$40 - 60^j$
TT Ari	0.57^k	$4 \times 10^{-9}^k$	$17 - 22.5^k$
V592 Cas	$1.4^{+1.0}_{-0.6}^l$		28^l
V795 Her	0.8^e	10^{-10}^e	41^e
AC Cnc			75.6^f
DW UMa			82^f
LX Ser			90^f
RR Pic			65^f
RW Tri			70.5^f
TV Col			70^f
UU Aqr			78^f
UX UMa			70^f
V348 Pup			81.1^f

Notes. First part is for systems with f_b detection, while second part is only for systems with red noise PDSs.

References. ^aGänsicke & Koester (1999), ^bGodon et al. (2008), ^cWolfe et al. (2013), ^dShafter (1983), ^eMizusawa et al. (2010), ^fRitter & Kolb (2003), ^gRodríguez-Gil et al. (2020), ^hHoard et al. (2004), ⁱLinnell et al. (2005), ^jLinnell et al. (2008), ^kBelyakov et al. (2010), ^lHuber et al. (1998)

maximum in f_b represents the observed maximum in m_{WD} is to fit the data in upper panel of Fig. 7 with a linear function. Unfortunately, the fits have too large errors mainly for the first coefficient defining correlation or anticorrelation¹⁰. Moreover, Dobrotka et al. (2020) mentioned that three possible groups of f_b could be present, but due to very low number of measurements it is not possible to confirm or reject the statement. Wijnen et al. (2015) theoretically studied m_{WD} distribution and they found three local maxima in simulated histograms. Therefore, a possibility that f_b distribution has more complicated structure has physical meaning. However, the histogram in Dobrotka et al. (2020) is constructed using well studied MV Lyr, V1504 Cyg and V344 Lyr cases where multi-components PDSs were found. Therefore, such histogram is contaminated by multiple measurements for one single m_{WD} . In such case the multiple structure of the histogram rather represents different sources of the fast variability with different f_b , and the potential correlation between m_{WD} and f_b would be for

¹⁰ Using all black data we got $m_{WD} = (-0.07 \pm 0.84)\log(f_b) + (-0.26 \pm 0.28) M_{\odot}$, while excluding the KR Aur case because of too scattered mass estimate we got $m_{WD} = (-0.81 \pm 1.05)\log(f_b) + (-0.49 \pm 0.34) M_{\odot}$. We did not use m_{WD} errors since they are not known for every system. Adding at least $0.1 M_{\odot}$ as error, the fit is even worse, i.e. the relative errors are larger or the direction get positive in the case of all black data.

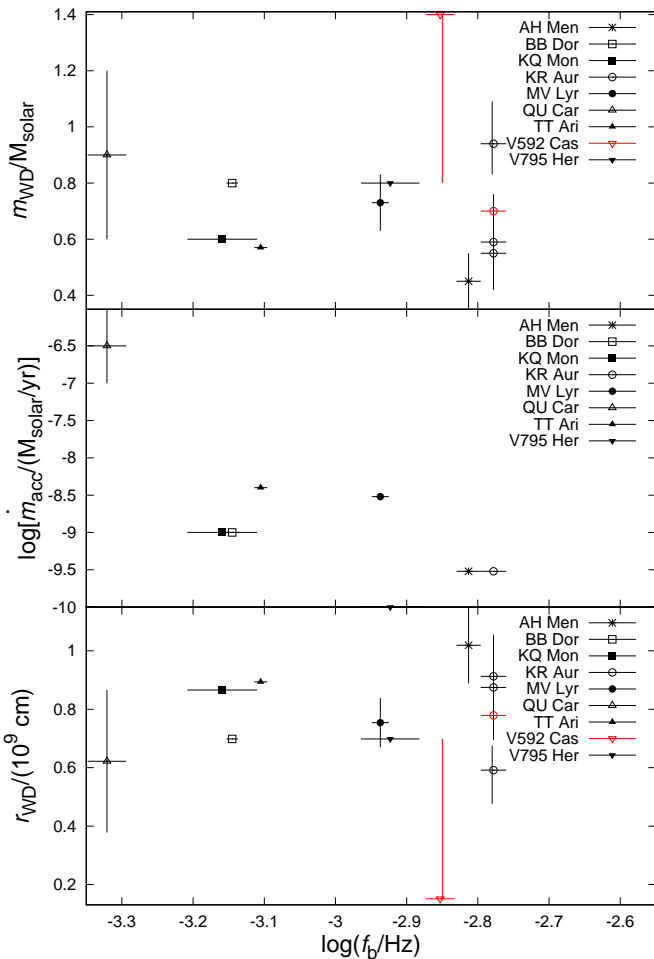


Fig. 7. m_{WD} (upper panel), \dot{m}_{acc} (middle panel) and r_{WD} (bottom panel) vs f_b from Table 1. Red color represents uncertain measurements.

only some specific f_b . MV Lyr and V1504 Cyg PDS show one dominant break and all other features are relatively weak. This dominant f_b seen in TESS data can be correlated with m_{WD} .

m_{WD} and its deeper potential well is not the only reason for higher temperature of the disc. Larger increased energy generation and subsequent stronger evaporation of matter into the corona can be produced by higher \dot{m}_{acc} too. Middle panel of Fig. 7 shows this case. We used values from Table 2. It seems that f_b decreases with increasing \dot{m}_{acc} . However, this correlation is based mainly on one single deviated point representing QU Car. Otherwise, the points does not show any significant correlation. Finally, both the m_{WD} and \dot{m}_{acc} together can play a role. Higher potential well of a massive WD and higher \dot{m}_{acc} can generate larger radius of an evaporated corona. For a detailed investigation much more systems needs to be studied.

The confirmation of corona scenario via such f_b vs system parameters correlation has very important consequence. As mentioned in the introduction, the ratio of X-ray to optical luminosity is of the order of 0.1 (Dobrotka et al. 2020) or even 0.01 - 0.001 (Balman et al. 2014). How is it then possible that X-rays are able to generate the observed optical radiation? Scaringi (2014) proposed reprocessing which apparently cannot work. An alternative must be searched elsewhere. The variability can be generated by

the corona. The reprocessing of X-rays from the corona generates only faint response. Such response can have a form of small side-lobes found in the shot profile by Dobrotka et al. (2019). The shot profile has another and dominant feature, the central spike. This has too large amplitude to be explainable by the reprocessing. It must originate directly from the central geometrically thin disc. The variability in the corona is generated by propagation of accretion fluctuations (Scaringi 2014). If these fluctuations somehow influence the underlying geometrically thin disc flow, the time scale of the optical flickering can have the same time scales. Such influence can be re-condensation of the corona back into the thin disc (Meyer et al. 2007). If the corona generates the $\log(f_b/\text{Hz}) = -3$ variability via mass accretion fluctuations, these fluctuations re-condensate and propagate in the thin disc. This can generate optical variability with the same frequency.

Finally, for authors identifying boundary layer as the source of the flickering it is important to relate f_b with the WD radius r_{WD} . We display such case in bottom panel of Fig. 7. For WD radius we used relation by Nauenberg (1972), hence the figure looks similar to the m_{WD} vs f_b case. Since the relation between m_{WD} and r_{WD} is not linear, the increase of r_{WD} with increasing f_b is accentuated yielding better linear fits than in the m_{WD} case. While the fits of m_{WD} vs f_b did not yield definite slope character (rising or declining) due to large parameter errors, the r_{WD} case is much better with clearly positive slope¹¹. However, the derivation of r_{WD} is not independent from the derivation of m_{WD} , and the "better" fits are just results of the non-linear transformation. Therefore, we can not conclude any fit "superiority", and the character of data is still uncertain and another measurements are needed as concluded for m_{WD} .

4.3. Detection vs non-detection of f_b

An indirect indication that the central disc region is the source of the studied flickering can be get from the discussion about detection vs non-detection of f_b . First idea is that the detection depends on the brightness of the binary. This is valid for systems with dominant white noise. Those systems have the lowest mean fluxes, therefore Poisson noise dominates the corresponding PDSs. However, all other systems with f_b detection or PDS dominated by red noise are equally distributed with no preferred fluxes except bright TT Ari and QU Car. These two systems have significantly higher fluxes, and f_b detection. But only two systems with specific flux does not say anything about any flux preference.

Apparently, the reason of detection vs non-detection must be searched elsewhere. The localisation of the flickering source can be the clue. If the source is the inner geometrically thin disc, either radiating directly or reprocessing X-rays from the central corona, it must be seen. This can be problematic in eclipsing systems or in systems with high inclination. In such conditions the central disc

¹¹ Using all black data we got $r_{WD} = (1.47 \pm 0.71)\log(f_b) + (0.23 \pm 0.24) 10^9 \text{ cm}$, while excluding the KR Aur case because of too scattered mass estimate we got $r_{WD} = (2.12 \pm 0.91)\log(f_b) + (0.43 \pm 0.30) 10^9 \text{ cm}$. Like in m_{WD} case we did not use errors because they are not known for every system, therefore the fit is just rough and orientational.

can be obscured by the outer disc edge. Investigating the inclinations (Table. 2) of systems with detected f_b we see that all have values below 75° . Taking the lower estimate of KQ Mon the inclinations are below 60° . On the other hand, systems with red noise PDSs are eclipsing like AY Psc (Szkody et al. 1989), BH Lyn (Andronov 1986; Richter 1989; Andronov et al. 1989), NSV 1907 (Hümmerich et al. 2017), or have higher inclinations (Table. 2). Clearly, the inclinations in red noise systems is higher than 65° . Therefore, there is a possible overlap of inclinations only in the cases of KQ Mon with the low end of red noise systems. Otherwise, the inclinations are very different implying that f_b is seen only in low inclination systems.

Another reason of missing f_b also related to the inner disc regions is the IP nature of the system. In these CVs the central disc is truncated, therefore missing, due to magnetic field of the WD. This is the case of for example RX J2133.7+5107 (Bonnet-Bidaud et al. 2006) where we see only red noise with clear spin frequency seen as one significantly deviated PDS bin. The PDS is not deformed like examples in the left panel of Fig. 2, therefore the red noise character is clear. V533 Her is a similar case with no f_b detection and being an IP candidate (Worpel et al. 2020). The PDS show ambiguous shape with not always present (variable from observation to observation) PDS structure near potential spin frequency of $\log(f/\text{Hz}) = -3.15$ (Rodríguez-Gil & Martínez-Pais 2002). We should exclude this binary from analysis like we did for examples in the left panel of Fig. 2, but since the spin frequency is not obvious we kept it. Anyhow, we did not get any f_b detection, therefore this case is also consistent with missing inner disc region in IPs.

Finally, worth to discuss is CP Pup case. The PDS is neither pure red noise neither a white noise. Red noise is clear up to approximately $\log(f/\text{Hz}) = -2.7$ to -3 , and a white noise plateau continues for higher frequencies. Szkody & Feinswog (1988) reported an inclination of 32° or 37° . Based on our inclination assumption, such system should show a clear f_b . However, the authors reported a potential WD mass of only $0.18 M_\odot$ for mass ratio of 1. Similar potential low mass of $0.12 M_\odot$ or $0.27 M_\odot$ concluded also Duerbeck et al. (1987). In the case of existing relation between f_b and m_{WD} and based on the characteristics of Fig. 7 the potential f_b (if present) can be outside of the studied frequency range for such low m_{WD} or can be hidden in the high frequency part of the PDS which is dominated by Poisson white noise. Therefore, CP Pup does not contradict the low inclination criterion for f_b detection, and thanks to its probable low m_{WD} it is a very suitable object for testing any relation between f_b and m_{WD} .

5. Summary and conclusions

Dobrotka et al. (2020) summarised characteristic f_b of the flickering in CVs. The authors found that it is very probable that PDSs of these systems have a preferred value close to $\log(f/\text{Hz}) = -3$ but only in high optical state. However, the probability of such a conclusion is only 69% (Dobrotka et al. 2021). It is still possible that the resulting histogram of measured f_b is the result of a random distribution. More measurements are needed to improve the statistics.

We selected nova-like CVs observed by TESS and we searched for f_b in PDSs. These systems are the majority

of their life-time in a high optical state. We selected uninterrupted light curve portions with durations of 5 and 10 days. We divided these portions into ten equally spaced subsamples and we calculated the mean PDSs. We focused our search on the frequency interval from $\log(f/\text{Hz}) = -3.5$ to -2.4 looking for the mentioned mHz f_b .

We found 15 positive detections, and the resulting histogram shows the searched preferred value (maximum) close to the $\log(f/\text{Hz}) = -3$. Thanks to the higher number of measurements compared to Dobrotka et al. (2020) we refined this value to the interval from $\log(f/\text{Hz}) = -2.95$ to -2.84 . The probability that this histogram maximum is not the result of just a random distribution is 96% in more conservative case. Apparently, this is much larger than previous value of 69%. Moreover, it is possible that the f_b is correlated with WD mass; the higher the mass, the lower the f_b . However, such a statement has only low confidence due to the still low number of studied systems with known WD mass and needs to be confirmed by further work. We need to increase the number of systems where the f_b is detected, and/or we should focus on systems with lower values close to $\log(f/\text{Hz}) = -3.5$ to populate empty region of the WD mass vs f_b parametric space.

As mentioned only 15 systems show clear f_b detection. All other objects have PDS dominated by white or red noise. While the white noise is the result of low brightness, the red noise is seen only in high inclination systems.

Both the inclination dependance and possible correlation between f_b and WD mass points to inner disc regions as the source of the detected f_b . This region is not well seen in high inclination systems or completely obscured in eclipsing CVs. The potential correlation between f_b and WD mass could be explained by inner hot corona as a source of f_b which is radially more extended for more massive WDs.

Acknowledgement

This work was supported by the Slovak grant VEGA 1/0576/24. We acknowledge with thanks the variable star observations from the AAVSO International Database contributed by observers worldwide and used in this research.

References

- Andronov, I. L. 1986, Astronomicheskij Tsirkulyar, 1418, 1
- Andronov, I. L., Kimeridze, G. N., Richter, G. A., & Smykov, V. P. 1989, Information Bulletin on Variable Stars, 3388, 1
- Arévalo, P. & Uttley, P. 2006, MNRAS, 367, 801
- Astropy Collaboration, Price-Whelan, A. M., Lim, P. L., et al. 2022, ApJ, 935, 167
- Astropy Collaboration, Price-Whelan, A. M., Sipőcz, B. M., et al. 2018, AJ, 156, 123
- Astropy Collaboration, Robitaille, T. P., Tollerud, E. J., et al. 2013, A&A, 558, A33
- Balman, S., Godon, P., & Sion, E. M. 2014, ApJ, 794, 84
- Balman, S. & Revnivtsev, M. 2012, A&A, 546, A112
- Baptista, R. & Bortoletto, A. 2004, AJ, 128, 411
- Baptista, R. & Bortoletto, A. 2008, ApJ, 676, 1240
- Belyakov, K. V., Suleimanov, V. F., Nikolaeva, E. A., & Borisov, N. V. 2010, in American Institute of Physics Conference Series, Vol. 1273, 17th European White Dwarf Workshop, ed. K. Werner & T. Rauch (AIP), 342–345
- Bonnet-Bidaud, J. M., Mouchet, M., de Martino, D., Silvotti, R., & Motch, C. 2006, A&A, 445, 1037
- Bruch, A. 1992, A&A, 266, 237
- Bruch, A. 1996, A&A, 312, 97
- Bruch, A. 2000, A&A, 359, 998
- Bruch, A. 2015, A&A, 579, A50

Bruch, A. 2022, MNRAS, 514, 4718
 Bruch, A. 2023a, MNRAS, 519, 352
 Bruch, A. 2023b, MNRAS, 525, 1953
 Dobrotka, A., Mineshige, S., & Ness, J.-U. 2014, MNRAS, 438, 1714
 Dobrotka, A., Negoro, H., & Konopka, P. 2020, A&A, 641, A55
 Dobrotka, A., Negoro, H., & Mineshige, S. 2019, A&A, 631, A134
 Dobrotka, A. & Ness, J.-U. 2015, MNRAS, 451, 2851
 Dobrotka, A., Ness, J.-U., & Bajčičáková, I. 2016, MNRAS, 460, 458
 Dobrotka, A., Ness, J.-U., Mineshige, S., & Nucita, A. A. 2017, MNRAS, 468, 1183
 Dobrotka, A., Orio, M., Benka, D., & Vanderburg, A. 2021, A&A, 649, A67
 Duerbeck, H. W., Seitter, W. C., & Duemmler, R. 1987, MNRAS, 229, 653
 Gänsicke, B. T. & Koester, D. 1999, A&A, 346, 151
 Godon, P., Sion, E. M., Barrett, P. E., Szkody, P., & Schlegel, E. M. 2008, ApJ, 687, 532
 Höshi, R. 1979, Progress of Theoretical Physics, 61, 1307
 Hameury, J. M. & Lasota, J. P. 2017, A&A, 602, A102
 Hoard, D. W., Linnell, A. P., Szkody, P., et al. 2004, ApJ, 604, 346
 Honeycutt, R. K. & Kafka, S. 2004, AJ, 128, 1279
 Horne, J. H. & Baliunas, S. L. 1986, ApJ, 302, 757
 Huber, M. E., Howell, S. B., Ciardi, D. R., & Fried, R. 1998, PASP, 110, 784
 Hümmerich, S., Gröbel, R., Hambsch, F.-J., et al. 2017, New A, 50, 30
 Kang, T. W., Retter, A., Liu, A., & Richards, M. 2006, AJ, 132, 608
 Kato, T., Ishioka, R., & Uemura, M. 2002, PASJ, 54, 1033
 Kotov, O., Churazov, E., & Gilfanov, M. 2001, MNRAS, 327, 799
 Linnell, A. P., Godon, P., Hubeny, I., et al. 2008, ApJ, 676, 1226
 Linnell, A. P., Szkody, P., Gänsicke, B., et al. 2005, ApJ, 624, 923
 Lyubarskii, Y. E. 1997, MNRAS, 292, 679
 Meyer, F., Liu, B. F., & Meyer-Hofmeister, E. 2007, A&A, 463, 1
 Meyer, F. & Meyer-Hofmeister, E. 1981, A&A, 104, L10
 Meyer, F. & Meyer-Hofmeister, E. 1994, A&A, 288, 175
 Mizusawa, T., Merritt, J., Ballouz, R.-L., et al. 2010, PASP, 122, 299
 Nauenberg, M. 1972, ApJ, 175, 417
 Ness, J., Starrfield, S., Burwitz, V., et al. 2003, ApJ, 594, L127
 Osaki, Y. 1974, PASJ, 26, 429
 Papadakis, I. E. & Lawrence, A. 1993, MNRAS, 261, 612
 Revnivtsev, M., Burenin, R., Bikmaev, I., et al. 2010, A&A, 513, A63
 Richter, G. A. 1989, Information Bulletin on Variable Stars, 3287, 1
 Ritter, H. & Kolb, U. 2003, A&A, 404, 301
 Rodriguez-Gil, P. & Martínez-Pais, I. G. 2002, MNRAS, 337, 209
 Rodriguez-Gil, P., Shahbaz, T., Torres, M. A. P., et al. 2020, MNRAS, 494, 425
 Sazonov, S., Revnivtsev, M., Burenin, R., et al. 2008, A&A, 487, 509
 Scargle, J. D. 1982, ApJ, 263, 835
 Scaringi, S. 2014, MNRAS, 438, 1233
 Scaringi, S., Körding, E., Groot, P. J., et al. 2013, MNRAS, 431, 2535
 Scaringi, S., Körding, E., Uttley, P., et al. 2012a, MNRAS, 427, 3396
 Scaringi, S., Körding, E., Uttley, P., et al. 2012b, MNRAS, 421, 2854
 Schreiber, M. R., Hameury, J. M., & Lasota, J. P. 2003, A&A, 410, 239
 Semena, A. N., Revnivtsev, M. G., Buckley, D. A. H., et al. 2014, MNRAS, 442, 1123
 Shafter, A. W. 1983, ApJ, 267, 222
 Smith, D. A. & Dhillon, V. S. 1998, MNRAS, 301, 767
 Szkody, P. & Feinswog, L. 1988, ApJ, 334, 422
 Szkody, P., Howell, S. B., Mateo, M., & Kreidl, T. J. 1989, PASP, 101, 899
 Van de Sande, M., Scaringi, S., & Knigge, C. 2015, MNRAS, 448, 2430
 van der Woerd, H., de Kool, M., & van Paradijs, J. 1984, A&A, 131, 137
 Warner, B. 1995, Cambridge Astrophysics Series, 28
 Wijnen, T. P. G., Zorotovic, M., & Schreiber, M. R. 2015, A&A, 577, A143
 Wolfe, A., Sion, E. M., & Bond, H. E. 2013, AJ, 145, 168
 Worpel, H., Schwope, A. D., Traulsen, I., Mukai, K., & Ok, S. 2020, A&A, 639, A17
 Zamanov, R. K. & Bruch, A. 1998, A&A, 338, 988
 Zorotovic, M., Schreiber, M. R., & Gänsicke, B. T. 2011, A&A, 536, A42

Appendix A: Additional tables

Tables A.1 and A.2 show all selected f_b values for $n_d = 10$ and $n_d = 5$, respectively.

Table A.1. Selected f_b for systems with positive detection using $n_d = 10$.

object	start (MJD)	log(f_b /Hz)						
AH Men	1325.297	-2.955(085)	1339.656	-2.773(051)	1424.554	-2.804(037)	1599.312	-2.896(069)
	1613.758	-2.795(034)	2144.514	-2.882(062)	2158.861	-2.753(055)	2144.514	-2.890(077)
	2158.861	-2.784(072)	2335.082	-2.724(066)	2335.078	-2.612(031)	2361.773	-2.967(101)
BB Dor	1327.816	-3.196(103)	1354.108	-3.094(072)	1368.601	-3.168(040)	1424.556	-3.184(051)
	1438.260	-3.185(041)	1451.620	-3.100(074)	1478.431	-3.140(033)	1491.903	-3.226(049)
	1505.013	-3.157(045)	1518.378	-3.196(073)	1545.205	-3.196(098)	2036.278	-3.255(056)
	2049.153	-3.233(056)	2075.156	-3.189(052)	2115.886	-3.080(039)	2130.210	-3.241(037)
	2144.516	-3.180(051)	2158.863	-3.143(043)	2174.230	-3.089(015)	2187.239	-3.071(069)
	2201.734	-3.058(047)	2215.435	-3.047(050)	2229.231	-3.180(038)	2242.585	-3.125(068)
	2282.712	-3.142(036)	2295.900	-3.242(059)	2361.771	-3.250(032)	2375.861	-3.174(087)
KQ Mon	2229.049	-3.177(059)	2242.403	-3.120(089)				
KR Aur	2474.172	-2.878(081)	2487.182	-2.894(081)	2500.394	-2.728(034)	2513.920	-2.796(070)
	2526.052	-2.788(029)	2540.164	-2.767(040)				
MV Lyr	1683.356	-3.077(039)	1697.347	-2.922(034)	2010.269	-3.094(048)	2023.117	-3.009(029)
	2390.656	-2.895(054)	2405.332	-2.925(041)	2419.992	-2.904(039)	2433.721	-2.850(021)
	2769.902	-2.994(104)	2810.874	-2.786(065)				
QU Car	2321.031	-3.204(047)	2347.302	-3.377(032)				
V504 Cen	2334.205	-2.911(058)	2347.305	-2.779(073)				
V592 Cas	1777.734	-2.888(032)	1957.269	-2.850(038)	1970.969	-2.811(036)		
V751 Cyg	2797.103	-2.992(038)	2810.874	-2.976(029)				
V795 Her	2010.271	-2.904(051)	2023.118	-2.957(068)				
V1193 Ori	1451.561	-3.017(068)	2174.234	-2.809(028)	2187.201	-2.862(029)		
HS 0506+7725	1816.088	-2.952(036)	1828.970	-2.816(027)	1842.507	-2.837(017)	1856.400	-2.944(090)
	1983.630	-3.060(065)	1996.914	-2.915(060)	2010.264	-2.935(047)		
TIC 92167387	2309.017	-3.026(096)	2322.400	-2.995(079)				

Notes. Start denotes the starting time of the selected light curve portion with MJD = JD - 2457000. The values in parenthesis represent the errors.

Table A.2. The same as Table A.1 but for $n_d = 5$.

object	start (MJD)	log(f_b /Hz)						
BB Dor	1332.816	-3.172(048)	1339.655	-3.119(104)	1368.601	-3.190(018)	1396.641	-3.075(069)
	1410.903	-3.075(070)	1424.556	-3.131(082)	1429.556	-3.193(070)	1438.260	-3.186(076)
	1443.260	-3.194(090)	1451.620	-3.094(062)	1468.273	-3.261(034)	1478.431	-3.234(077)
	1483.432	-3.088(043)	1496.905	-3.084(040)	1505.013	-3.211(049)	1510.014	-3.102(099)
	1518.378	-3.170(032)	1534.998	-3.302(046)	1558.541	-3.168(050)	1573.258	-2.996(062)
	1587.151	-3.128(090)	1673.056	-3.161(083)	2049.153	-3.173(074)	2061.851	-3.179(036)
	2080.156	-3.211(077)	2088.240	-3.166(095)	2102.328	-3.091(071)	2115.886	-3.195(069)
	2120.886	-3.080(072)	2130.210	-3.020(102)	2135.210	-3.257(080)	2144.516	-3.146(034)
	2149.516	-3.134(044)	2158.863	-3.195(072)	2163.863	-3.046(064)	2174.230	-3.145(084)
	2179.230	-3.191(042)	2201.734	-2.993(065)	2206.735	-3.067(043)	2215.435	-2.967(082)
	2220.436	-3.245(050)	2234.232	-3.195(084)	2282.712	-3.060(053)	2287.713	-3.152(036)
	2295.900	-3.248(047)	2300.902	-3.170(090)	2323.765	-3.136(077)	2337.353	-3.065(058)
	2351.849	-3.166(064)	2361.771	-3.383(035)	2366.771	-3.168(055)	2375.861	-3.183(086)
	2964.040	-3.054(058)	2969.550	-3.096(070)	2982.406	-3.127(054)	2989.842	-3.149(032)
	2995.098	-3.083(042)	3007.750	-3.096(065)	3015.381	-2.948(065)	3021.403	-3.093(075)
	3028.757	-3.085(062)	3034.306	-3.049(078)	3041.114	-3.075(070)	3083.690	-3.096(094)
	3112.190	-3.179(063)	3126.641	-3.095(093)	3155.045	-3.326(039)	3168.617	-3.162(075)
	3182.502	-3.064(064)						
KQ Mon	2229.049	-3.151(050)	2234.049	-3.332(049)	2242.403	-3.097(099)	2247.406	-3.130(095)
MV Lyr	1683.356	-2.942(047)	1688.358	-2.995(075)	1697.347	-2.950(054)	1702.348	-2.949(042)
	2010.269	-3.137(034)	2015.270	-3.095(087)	2023.117	-3.096(046)	2028.117	-2.996(095)
	2390.656	-2.893(044)	2395.656	-2.894(081)	2405.332	-2.926(055)	2410.332	-2.903(037)
	2419.992	-2.868(022)	2424.993	-2.894(045)	2433.721	-2.850(033)	2438.723	-2.827(029)
	2774.902	-2.935(031)	2783.534	-2.931(077)	2810.874	-2.785(054)		
TT Ari	2447.693	-3.002(056)	2461.243	-3.048(041)	2474.183	-2.982(042)	2487.186	-3.090(030)
	2492.187	-3.057(034)	3208.791	-3.117(044)	3221.701	-3.096(037)	3227.661	-3.141(029)
	3235.439	-3.092(038)	3240.714	-3.138(015)	3253.592	-3.116(057)		
V504 Cen	2334.205	-2.995(082)	2339.205	-2.966(069)				
V592 Cas	1764.688	-2.826(039)	1777.734	-2.823(042)	1782.734	-2.886(016)	1957.269	-2.804(060)
	1962.271	-2.848(049)	1970.969	-2.750(045)	1975.969	-2.864(032)	2853.358	-2.906(038)
	2867.465	-2.953(032)	2874.823	-2.905(040)	2883.011	-2.915(040)	2889.639	-2.893(047)
	2897.224	-2.894(035)	2903.600	-2.910(036)				
V704 And	1777.735	-2.979(071)	2853.359	-2.812(053)	2867.466	-2.979(042)	2874.823	-2.973(049)
V751 Cyg	1711.368	-3.109(074)	1724.944	-3.096(081)	2797.103	-2.923(061)	2802.104	-3.064(038)
	2810.874	-2.967(050)	2815.874	-2.945(026)	2831.944	-2.995(087)		
V795 Her	1988.187	-2.967(080)	2001.467	-2.928(044)	2010.271	-2.904(085)	2015.272	-2.936(062)
	2028.119	-2.896(029)						
V1193 Ori	1456.561	-2.956(100)	2174.234	-2.752(033)	2179.234	-2.832(020)	2187.201	-2.902(025)
	2192.201	-2.946(045)						
HS 0506+7725	1816.088	-3.019(034)	1821.088	-3.099(077)	1828.970	-2.863(066)	1833.970	-2.837(039)
	1842.507	-2.761(033)	1847.509	-2.913(034)	1856.400	-2.842(025)	1983.630	-2.957(067)
	1988.633	-2.975(068)	1996.914	-2.977(062)	2001.916	-2.845(047)	2015.266	-2.926(025)
	2023.111	-2.797(064)	3292.486	-3.096(073)	3306.197	-2.957(081)		